Chemical short-range disorder in lithium oxide cathodes

Wang, Qidi; Yao, Zhenpeng; Wang, Jianlin; Guo, Hao; Li, Chao; Zhou, Dong; Bai, Xuedong; Li, Hong; Li, Baohua; Wagemaker, Marnix

Important note
To cite this publication, please use the final published version (if applicable).
Please check the document version above.

Article

Chemical short-range disorder in lithium oxide cathodes

Qidi Wang[1,9 ✉], Zhenpeng Yao[2,9], Jianlin Wang[3], Hao Guo[4], Chao Li[5], Dong Zhou[6], Xuedong Bai[3], Hong Li[7 ✉], Baohua Li[8 ✉], Marnix Wagemaker[1 ✉] & Chenglong Zhao[1 ✉]

Ordered layered structures serve as essential components in lithium (Li)-ion cathodes[1–3]. However, on charging, the inherently delicate Li-deficient frameworks become vulnerable to lattice strain and structural and/or chemo-mechanical degradation, resulting in rapid capacity deterioration and thus short battery life[2,4]. Here we report an approach that addresses these issues using the integration of chemical short-range disorder (CSRD) into oxide cathodes, which involves the localized distribution of elements in a crystalline lattice over spatial dimensions, spanning a few nearest-neighbour spacings. This is guided by fundamental principles of structural chemistry and achieved through an improved ceramic synthesis process. To demonstrate its viability, we showcase how the introduction of CSRD substantially affects the crystal structure of layered Li cobalt oxide cathodes. This is manifested in the transition metal environment and its interactions with oxygen, effectively preventing detrimental sliding of crystal slabs and structural deterioration during Li removal. Meanwhile, it affects the electronic structure, leading to improved electronic conductivity. These attributes are highly beneficial for Li-ion storage capabilities, markedly improving cycle life and rate capability. Moreover, we find that CSRD can be introduced in additional layered oxide materials through improved chemical co-doping, further illustrating its potential to enhance structural and electrochemical stability. These findings open up new avenues for the design of oxide cathodes, offering insights into the effects of CSRD on the crystal and electronic structure of advanced functional materials.

Lithium (Li)-containing transition metal oxides (Li_xTMO_2) have attracted a lot of interest because of their diverse compositions and structures that provide tunable electrochemical performance as electrodes in Li-ion batteries[1]. However, the occurrence of phase transitions on charging, usually leads to detrimental structural changes, limiting the amount of Li that can be extracted and thereby compromising the specific energy[2,4]. These challenges have limited the achievement of high-performance batteries and fundamental scientific understandings. Chemical short-range atomic arrangement represents the local structural heterogeneities with respect to the long-range average crystal structure, forming particular inter-atomic environments[5,6]. In recent years, this crystallographic phenomenon has attracted attention because it provides an opportunity to modify the crystal structure at the atomic level and control the structure–property relationships across a range of materials[7–10]. The exploration of chemical short-range atomic arrangement has provided insights into multiple-principal-element medium- and high-entropy alloys, which demonstrates notable

alterations in mechanical and structural properties[9,10]. Therefore, a new field is emerging in exploring the potential of modifying the local atomic arrangement at the nanometre scale in oxide cathodes. It has been suggested that the specific migration of transition metal ions could affect the local structure, improving ion transport and the performance of the material[11]. In this work, we show how the introduction of a specific atomic arrangement, referred to as chemical short-range disorder (CSRD), provides opportunities for tuning the structural properties of Li-ion layered electrodes, thereby improving their functional properties.

Screening Li-containing $LiMeO_2$ for CSRD

To explore the CSRD in oxide cathodes, we take advantage of the structural chemistry of Li-containing oxides, conducting a comprehensive examination of various compositions and their potential existence in diverse structures. This offers an opportunity to identify the possible

[1]Department of Radiation Science and Technology, Delft University of Technology, Delft, The Netherlands. [2]The State Key Laboratory of Metal Matrix Composites, Center of Hydrogen Science, School of Materials Science and Engineering, Shanghai Jiao Tong University, Shanghai, China. [3]State Key Laboratory for Surface Physics, Institute of Physics, Chinese Academy of Sciences, Beijing, China. [4]Neutron Scattering Laboratory, Department of Nuclear Physics, China Institute of Atomic Energy, Beijing, China. [5]Shanghai Key Laboratory of Magnetic Resonance, School of Physics and Electronic Science, East China Normal University, Shanghai, China. [6]Helmholtz-Zentrum Berlin für Materialien und Energie, Berlin, Germany. [7]Key Laboratory for Renewable Energy, Institute of Physics, Chinese Academy of Sciences, Beijing, China. [8]Shenzhen Key Laboratory on Power Battery Safety and Shenzhen Geim Graphene Center, School of Shenzhen International Graduate, Tsinghua University, Shenzhen, China. [9]These authors contributed equally: Qidi Wang, Zhenpeng Yao. ✉e-mail: q.wang-11@tudelft.nl; hli@iphy.ac.cn; libh@mail.sz.tsinghua.edu.cn; m.wagemaker@tudelft.nl; c.zhao-1@tudelft.nl
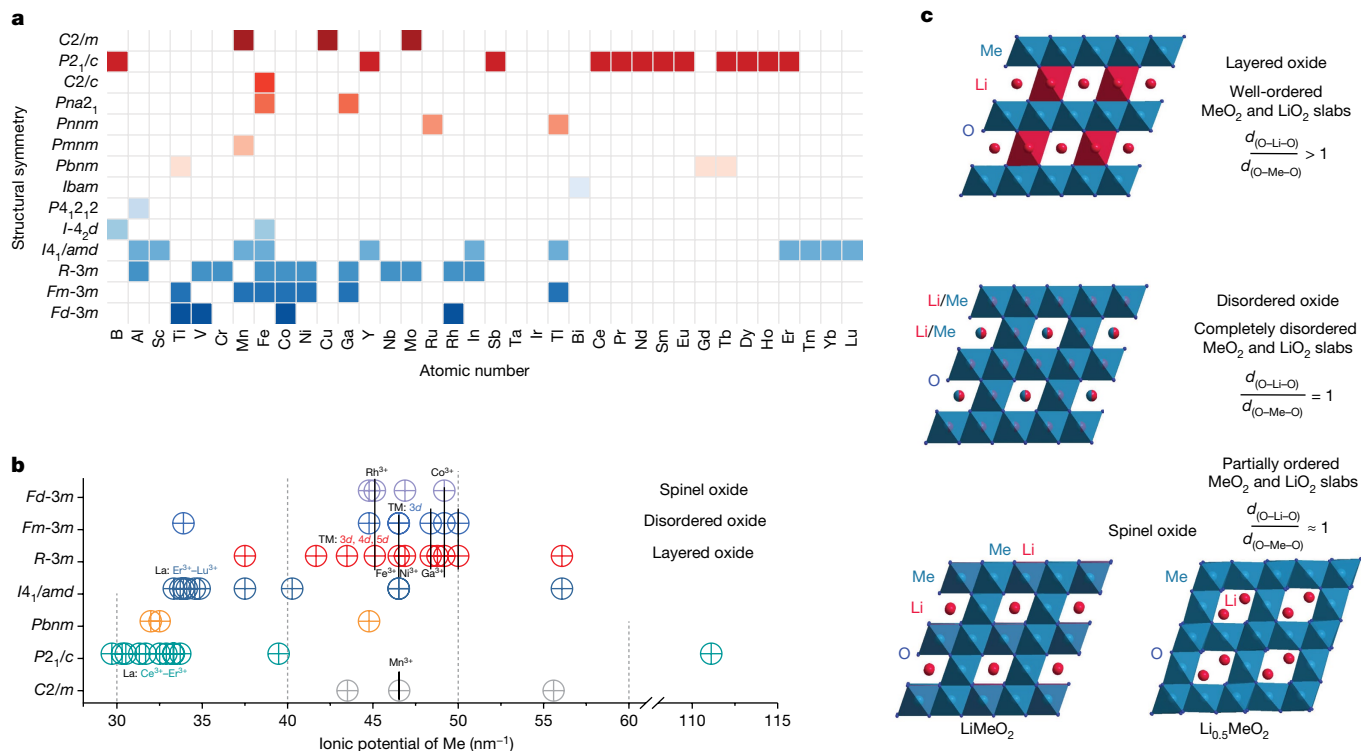
Article

Fig. 1 | Screening the crystal structure of LiMeO₂ compositions. a, Structural symmetry of LiMeO₂ compositions. Me is the trivalent metal ion (Supplementary Figs. 1–14 and Supplementary Tables 1 and 2). **b**, Ionic potential of Me ions in LiMeO₂ compositions. **c**, Structure transformation in layered, disordered and spinel oxides, and their corresponding $d_{(O-Li-O)}/d_{(O-Me-O)}$, where $d_{(O-Li-O)}$ is the Li layer distance and $d_{(O-Me-O)}$ is the Me layer distance. The spinel structure of $LiMe^{3+}O_2$ differs from $Li_{0.5}Me^{3.5+}O_2$, in which Li is stabilized in tetrahedral sites because of the stronger electrostatic repulsion from Me ions in a higher average valence of 3.5+.

compositions for preparing these materials from the most fundamental starting point. After screening compositions with the general formula LiMeO₂ (Me indicates metal element) in the inorganic crystal structure database, 36 different Me^{3+} ions are identified that can participate in forming LiMeO₂ oxides within about 14 space groups (Fig. 1a, Supplementary Figs. 1–14 and Supplementary Table 1). This compositional space is huge and complex. Thus, it is helpful to find a quantitative parameter to signify this relationship between chemical composition and the corresponding crystal structure. For the Li–Me–O system, the nature of the Me ions is decisive for the crystal structures, because their hybridizations with oxygen are stronger than that between Li-ion and oxygen[12]. Here the ionic potential (Φ) of Me ions, defined as the charge number (n) over the ion radius (R) (ref. 13), can be considered a representative parameter to quantitatively describe the properties of various compositions[12,14], providing guidance for composition–structure identification within specific ranges. Moreover, the advantages of this approach become increasingly evident when extending it to multiple-principal-element systems, through the weighted-average ionic potential of Me ions, $\overline{\Phi_{Me}}$, defined as $\overline{\Phi_{Me}} = \sum \frac{w_i n_i}{R_i}$ (w_i is the content of Me_i having charge number n_i and radius R_i).

The relationship between the ionic potential of Me^{3+} ions and the crystal structure of LiMeO₂ oxides is shown as a phase map in Fig. 1b. Different structures emerge across specific ranges of ionic potential, demonstrating potential quantitative relationships and providing references for the design of multiple-element systems. Specifically, Me^{3+} ions suitable for cathodes are identified in the ionic potential range of 45–50 nm⁻¹, in which several ions are observed existing in different polymorphs in the LiMeO₂ composition (Fig. 1b and Supplementary Figs. 12–14). This seems to be relevant in the context of the short-range atomic arrangement, which is more likely to occur for compositions that can lead to multiple structures. As shown in Fig. 1b, Fe^{3+}, Ni^{3+} and

Ga^{3+} exhibit layered and disordered structures, Rh^{3+} forms layered and spinel structures and Co^{3+} demonstrates all three structures. Generally, these polymorphisms are associated with different synthesis conditions[15–17], in which the crystal lattices can transform from one structure to the other under specific conditions (Fig. 1c and Supplementary Note 1). This suggests that introducing CSRD structure in materials could be available by altering the chemical composition and/or the synthesis conditions[10,18,19].

For instance, owing to the high structural diversity of LiCoO₂, as well as the lack of any filled antibonding states, Co^{3+} (d^6) has a high octahedral stability in layered, disordered and spinel structures[20] (Supplementary Fig. 15a). These phases are frequently referenced by the temperature required for their synthesis[15], leading to varied properties (Supplementary Fig. 15b). The layered structure necessitates a higher synthesis temperature (around 900 °C) compared with the spinel form (around 400 °C), and it is dominantly used as cathodes for a higher intercalation voltage[21,22]. Despite their different synthesis temperatures, the calculated free energies are similar with −5.689 eV per atom and −5.688 eV per atom, respectively. Furthermore, the disordered rock-salt structure can form during the synthesis of the layered phase[23] (Supplementary Fig. 15c). These observations suggest that it is possible to prepare an intermediate phase as a CSRD structure in layered LiCoO₂ by optimizing the synthesis conditions.

Crystal structure of CSRD–LiCoO₂

Aiming at introducing CSRD arrangements in layered LiCoO₂, a survey of different parameters was conducted, including the annealing temperature, time, gas environment, various precursors and their ratios. The final material is obtained with LiOH·H₂O and Co(OH)₂ at a molar ratio of 1.03:1 by first heating at 700 °C in air and subsequently calcining
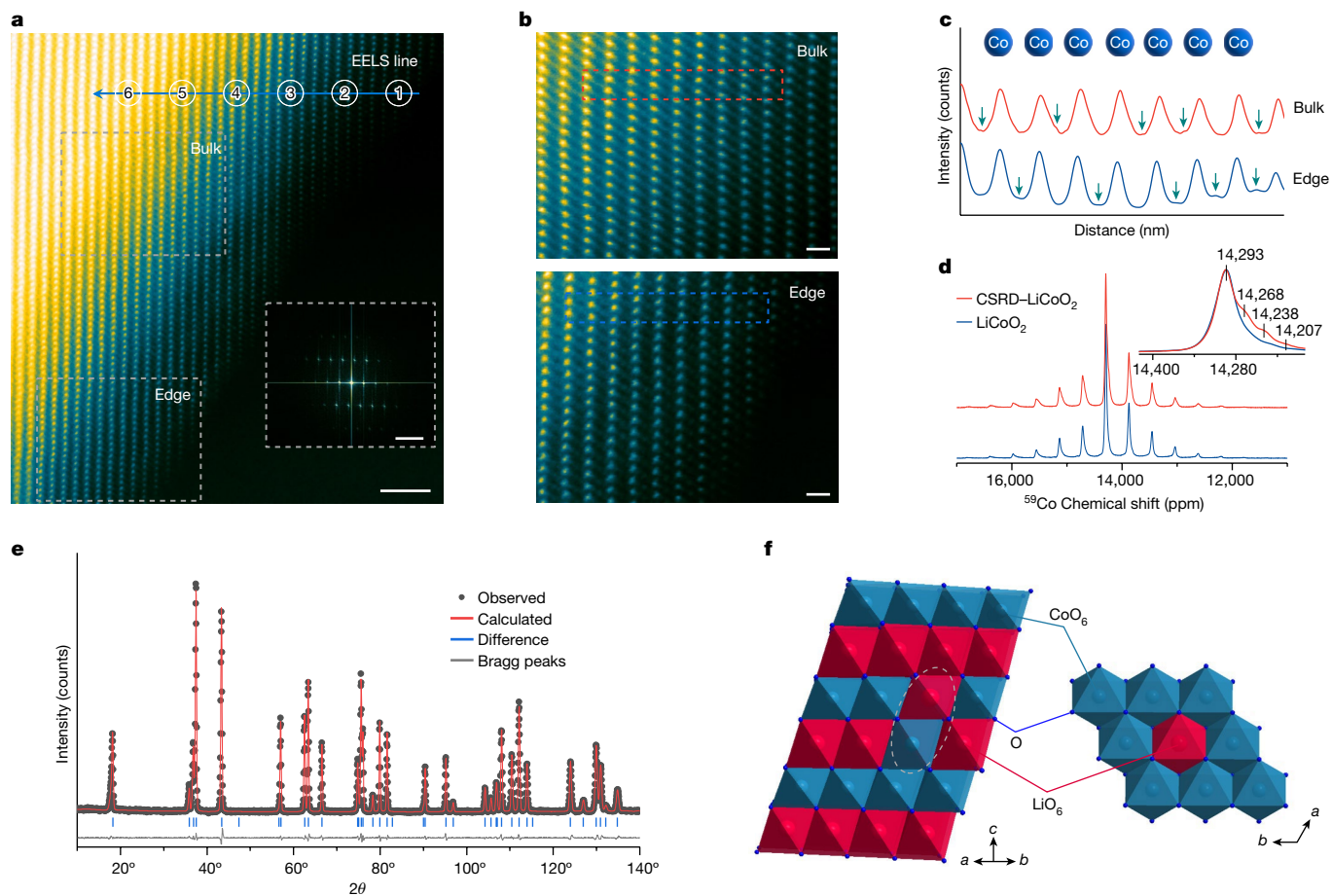
Fig. 2 | CSRD configuration of LiCoO₂. a, Atomic-resolution STEM-HAADF image and the corresponding FFT pattern (inset) of the as-prepared CSRD–LiCoO₂ material. **b**, The magnified bulk and edge regions from **a**. **c**, Line profiles along the horizontal direction of the bulk and edge regions, in which the green arrows denote the local short-range disorder distribution of Co. **d**, Solid-state

^{59}Co MAS-NMR spectra of LiCoO₂ materials. Inset, additional bands of the as-prepared CSRD–LiCoO₂ material. **e**, NPD pattern of the as-prepared CSRD–LiCoO₂ material recorded at a temperature of 300 K. **f**, Crystal structure of the corresponding CSRD–LiCoO₂ structure. Scale bars, 2 nm (**a**), 5 nm⁻¹ (**a**, inset); 0.5 nm (**b**).

at 1,000 °C in an O_2 atmosphere. X-ray powder diffraction (XRD) pattern of the as-synthesized material corresponds to an O3-type structure with a higher intensity of (104) reflection than that of the regular material (Supplementary Fig. 16a). The particle size is larger, having a spherical particle shape (Supplementary Fig. 16b). Atomic-resolution high-angle annular dark field of scanning transmission electron microscopy (STEM-HAADF) and the corresponding fast Fourier transform (FFT) pattern also indicate that this as-prepared LiCoO₂ material is indexed as the layered structure (Fig. 2a). However, in the magnified bulk and edges of the HAADF images (Fig. 2b), several locations show a different contrast in Li layer, suggesting the presence of Co ions. The line profiles further support the presence of Co ions in Li layers (Fig. 2c). Moreover, this structure is confirmed by the focused ion beam (FIB)-STEM measurements (Supplementary Fig. 16c,d), which suggests this phenomenon is the bulk information. Conversely, regular LiCoO₂ does not show the disorder phenomenon (Supplementary Fig. 16e). Electron energy loss spectroscopy (EELS) is also carried out to investigate the oxidation states of Co ions and oxygen from the edge of the grain towards the bulk (Supplementary Fig. 16f,g), which shows that the existing CSRD structure does not affect their valence. Solid-state ^{59}Co magic-angle spinning nuclear magnetic resonance (MAS-NMR) spectra are recorded to characterize the Co local environments (Fig. 2d). The CSRD material exhibits three new signals at around 14,207 ppm, 14,238 ppm and 14,268 ppm apart from the signal at around 14,293 ppm, which can be assigned to the various second (Li_nCo_{6-n}) neighbour environments[24], showing the changes in the local atomic arrangement. Inductively coupled plasma

optical emission spectrometry (ICP-OES) is then conducted, resulting in about $Li_{1.0}CoO_2$. Based on the above, neutron powder diffraction (NPD) is performed for its higher sensitivity towards Li and Co distribution owing to the opposite sign of neutron scattering lengths, −1.9 fm and 2.49 fm, respectively. Starting with a structural model having Li/Co disorder (Fig. 2e,f and Supplementary Tables 3 and 4), the refinement indicates about 2.6% Co resides in Li layers, which is held responsible for the CSRD structure. Moreover, the ratio of $d_{(O-Li-O)}/d_{(O-Me-O)}$ from the refinement for this CSRD–LiCoO₂ results in about 1.287, which is smaller than about 1.295 of the regular LiCoO₂, approaching the smaller ratio of the disordered and spinel oxides. $d_{(O-Li-O)}$ is the interlayer distance of Li layer and $d_{(O-Me-O)}$ is Me layer distance[25].

Electrochemistry of CSRD–LiCoO₂ cathode

The electrochemical properties were examined by pairing the regular and CSRD–LiCoO₂ cathode with a metallic Li anode. When cycled at 0.1 C, both cathodes deliver a specific capacity of around 178 mAh g⁻¹; however, the corresponding dQ/dV indicates different phase transition behaviour (Fig. 3a,b). At the onset of charge, the regular LiCoO₂ exhibits a higher oxidation potential than that of the CSRD–LiCoO₂, which results from an insulator–metal transition associated with the first-order phase transition[4,26]. When further charged to around 4.15 V, reaching about $Li_{0.5}CoO_2$, a phase transition of Li⁺ and vacancy ordering appears for the regular LiCoO₂, corresponding to a hexagonal to monoclinic structure transition[4]. However, this transition is not
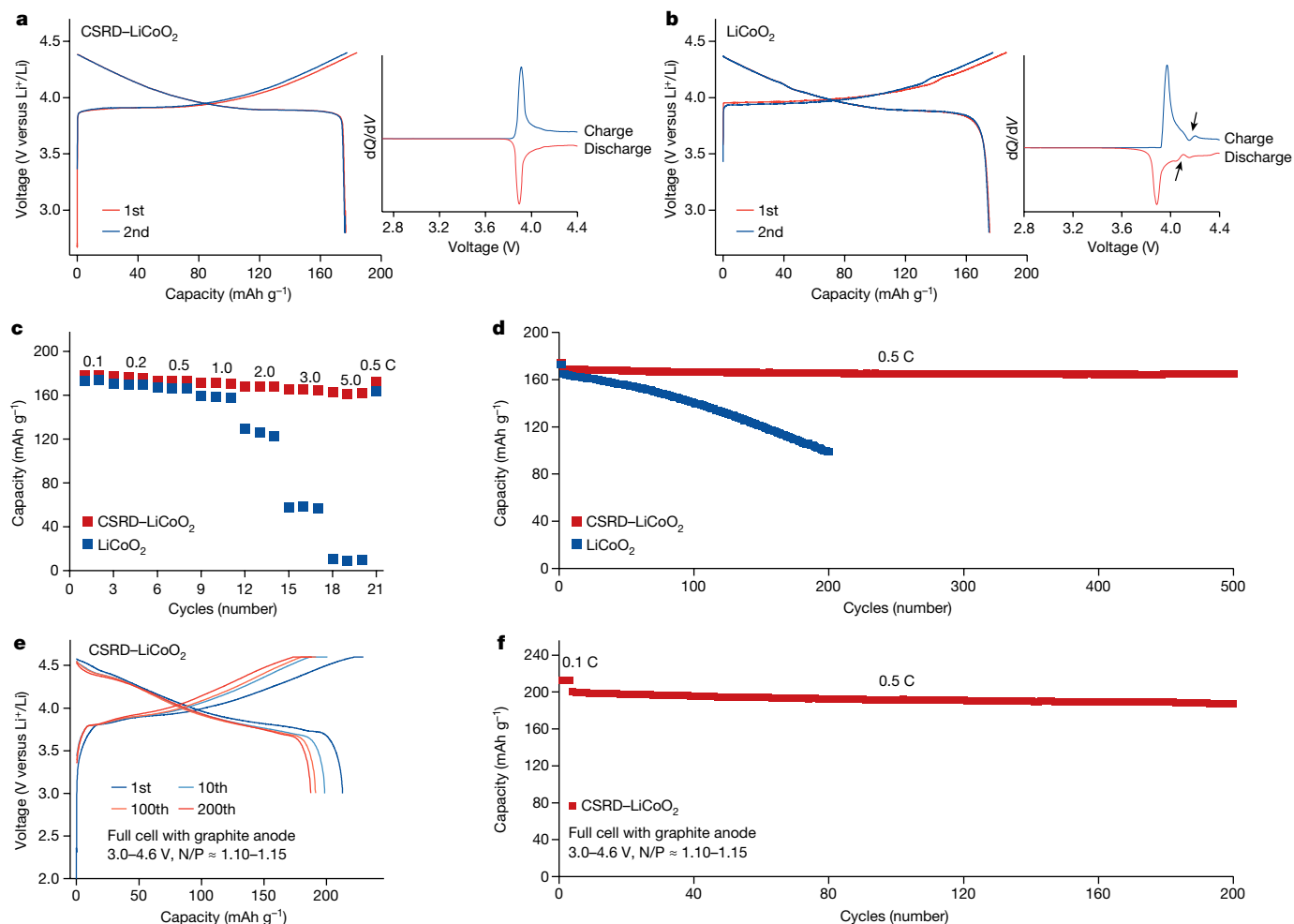
Fig. 3 | Electrochemical performance. a,b, Galvanostatic charge–discharge curves and the corresponding dQ/dV curves of the CSRD–LiCoO$_2$ cathode (**a**) and the regular LiCoO$_2$ cathode (**b**) at the voltage range of 2.8–4.4 V at 0.1 C rate. **c**, Electrochemical rate capabilities cycled between 2.8 V and 4.4 V. **d**, Cycling performance at 0.1 C rate for two cycles before cycling at 0.5 C between 2.8 V and 4.4 V. **e**, Galvanostatic charge–discharge curves. **f**, Capacity retention of CSRD–LiCoO$_2$ and graphite full cells cycled between 3.0 V and 4.6 V.

observed in the CSRD–LiCoO$_2$ (Fig. 3a), evidencing different structural transition characteristics. Galvanostatic intermittent titration technique measurements were conducted to further understand the Li-ion insertion–extraction properties (Supplementary Figs. 17a–c), in which the relatively low voltage polarization and high Li-ion diffusion coefficients are held responsible for the good rate and cycling capabilities of the CSRD–LiCoO$_2$. When cycled at higher rates of 1.0 C and 5.0 C (Fig. 3c and Supplementary Fig. 17d,e), CSRD–LiCoO$_2$ cathode exhibits higher capacity retention, amounting to 172 mAh g^{-1} and 162 mAh g^{-1} in comparison with the regular LiCoO$_2$ amounting to 159 mAh g^{-1} and 10 mAh g^{-1}, respectively. Long-term cycling stabilities of CSRD–LiCoO$_2$ cathode are investigated at a 0.5 C rate, at which the capacity retention is approximately 97% after 500 cycles with approximately 99.9% Coulombic efficiency (Fig. 3d and Supplementary Fig. 17f). These properties demonstrate competitive advantages compared with the regular cathode that shows a capacity retention of approximately 57% after 200 cycles under the same conditions. The higher rate capabilities of CSRD–LiCoO$_2$ cathode are further evaluated up to 12.0 C, showing a capacity of around 131 mAh g^{-1} (Supplementary Fig. 17g,h); and after rate cycling, a reversible capacity of around 174 mAh g^{-1} can be recovered at 0.5 C. The galvanostatic charge–discharge performance cycled in the voltage range of 2.8–4.5 V compared with Li$^+$/Li is further examined (Supplementary Fig. 18a,b). CSRD–LiCoO$_2$ cathode exhibits a reversible capacity of about 195 mAh g^{-1}, slightly larger than that of the

regular LiCoO$_2$ cathode having a capacity of 190 mAh g^{-1}, and after 200 cycles the capacity retention of the CSRD–LiCoO$_2$ is 88% larger than that of the regular LiCoO$_2$ (Supplementary Fig. 18c). Furthermore, cycling performance of CSRD–LiCoO$_2$ cathode at a higher cutoff voltage of 4.7 V has been evaluated (Supplementary Fig. 18d,e). A specific capacity of around 230 mAh g^{-1} is delivered at 0.1 C and a capacity retention of approximately 87% is obtained at a 0.5 C rate after 200 cycles. Moreover, full cells combining CSRD–LiCoO$_2$ and graphite are investigated as shown in Fig. 3e,f. When cycled at 0.5 C rate between 3.0 V and 4.6 V, full cells show a reversible capacity of approximately 200 mAh g^{-1} and the capacity retention of approximately 92.5% after 200 cycles. These results indicate that this CSRD–LiCoO$_2$ cathode has enhanced electrochemical properties. However, it should be noted that when charged to higher voltage (>4.5 V), ensuring the stability of electrode interfaces is important. Therefore, incorporating strategies such as trace doping[27], surface coatings[28] or electrolyte modifications[29] are recommended to further enhance the stability of electrode interfaces.

Structure evolution

To obtain insights into the structural evolution and the specific influence of this short-range atomic arrangement on cathodes, an in situ XRD test was performed (Fig. 4a and Supplementary Fig. 19). At the onset of the charge, both the regular and CSRD–LiCoO$_2$ cathodes go through
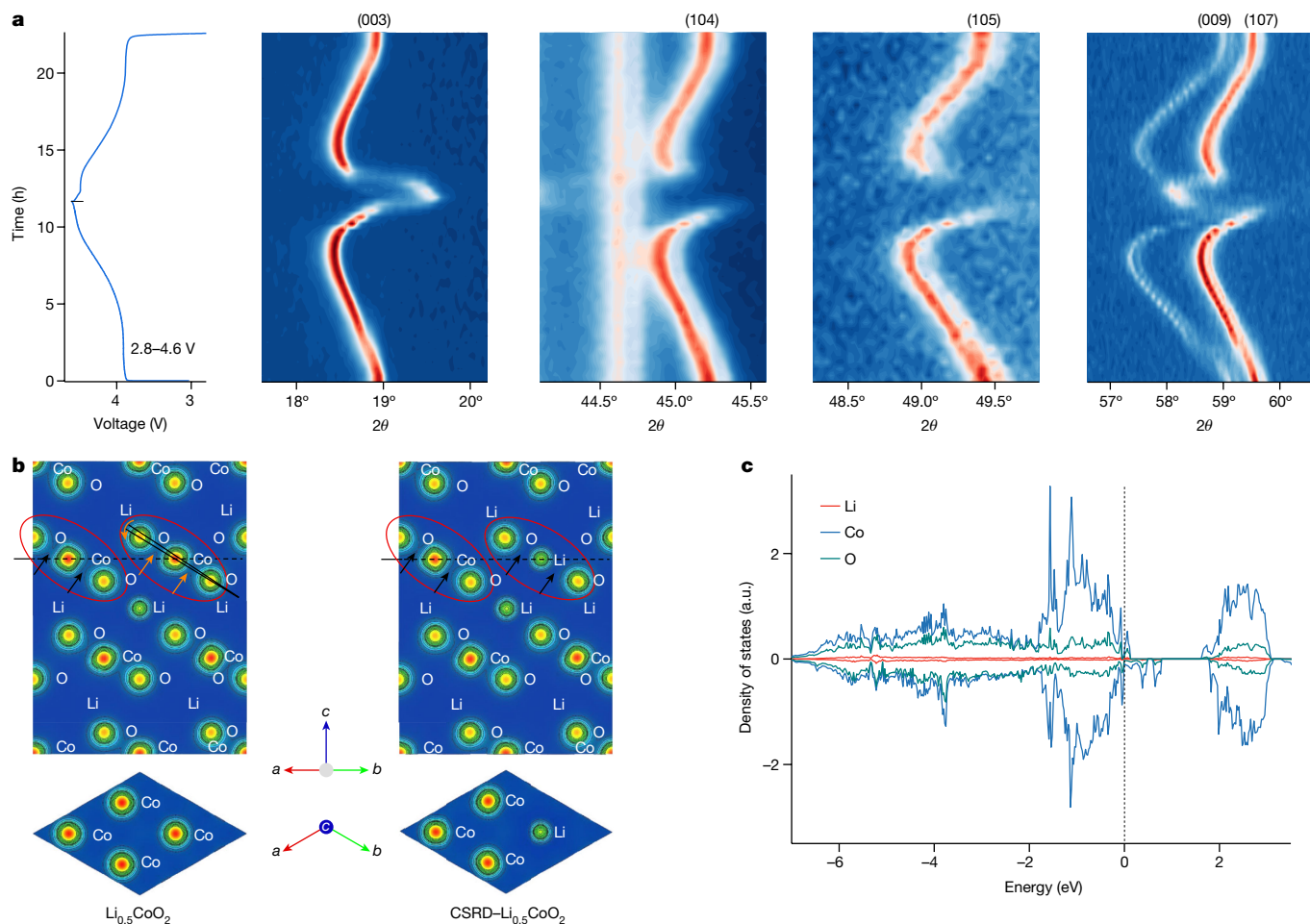
Fig. 4 | Crystal and electronic structure information of the CSRD−LiCoO₂ cathode. a, In situ XRD patterns recorded at a current rate of 0.08 C in the voltage range of 2.8–4.6 V. **b,** Charge density distribution of the CSRD−LiCoO₂ and the regular LiCoO₂ cathodes after the de-lithiation to $Li_{0.5}CoO_2$. The red contour indicates high charge density and the blue contour low charge density. **c,** PDOS of the CSRD−LiCoO₂ material. The dashed line represents the Fermi level at 0 eV.

the O3 to O3′ phase transition, associated with an insulator–metal transition[4,26]. Compared with the regular LiCoO₂, the CSRD−LiCoO₂ shows a smoother structural evolution in the phase coexistence region. When further charged to around 4.15 V, with nearly half of the Li being removed, the regular LiCoO₂ shows a clear Li⁺/vacancy ordering phase transition from the hexagonal to the monoclinic phase[4,30], resulting in the splitting of the (104), (105) and (107) reflections (Supplementary Fig. 19). By contrast, the CSRD−LiCoO₂ does not show these splitting, consistent with the above dQ/dV results (Fig. 3a), which indicates that the order–disorder transition is eliminated. At charging to 4.6 V, the CSRD−LiCoO₂ shows a relatively smaller (003) peak shift of 19.68° than 19.79° of the regular LiCoO₂, which could be because of the suppressed O3 to H(1−3) phase transition[31,32]. On discharging, the CSRD−LiCoO₂ presents a more symmetric structural evolution to the charge, explaining the more reversible capacity during extended cycling. These results show that although both LiCoO₂ share the initial O3-type structure, they show distinctly different structure evolutions, which could be responsible for the electrochemical performance.

The fundamental impact of the short-range atomic arrangement is then studied using first-principles density functional theory (DFT) calculations (Fig. 4b and Supplementary Fig. 20a). For the pristine composition of $Li_{1.0}CoO_2$, the charge density distribution shows a weak Co−O interaction in both configurations (Supplementary Fig. 20a). However, after de-lithiation to $Li_{0.5}CoO_2$, with the oxidation state of Co ions increasing to 3.5+, results in relatively stronger Co−O bonding and thus to more compact [CoO₆] octahedra and twisted CoO₂ slabs in the regular LiCoO₂ (Fig. 4b). By introducing the local disorder, this structural change is released in the CSRD−LiCoO₂ to some extent, in which the weaker Li−O interaction reduces the local strain in several neighbouring coordination layers. Meanwhile, the presence of Co in Li-ion layers can increase the interaction with adjacent oxygens, making it more difficult for the layers to slide, hence suppressing the phase transition that occurs in the ordered LiCoO₂. Moreover, the introduction of the short-range atomic disorder can alter the electronic structure of the cathode (Fig. 4c and Supplementary Fig. 20b), effectively closing the bandgap, and thus enhancing electronic conductivity. This is consistent with the aforementioned phase transition, indicating that this disorder plays an important part in the crystal and electronic structure of the material.

To evaluate if this CSRD approach is generally applicable to other oxide materials, we verify its application to the multiple-principal-element $Li_xMe_yO_2$ system, where Me can be a mixture of various elements (Supplementary Figs. 21 and 22, Supplementary Note 2 and Supplementary Tables 5–8). The result indicates that the introduction of CSRD structure can effectively increase the cycling stability of high-Ni layered cathodes (for example, $LiNi_{0.8}Co_{0.1}Mn_{0.1}O_2$).

Outlook of CSRD in Li-ion oxides

Chemical short-range atomic arrangements are recognized in materials science and engineering, presenting an opportunity to tailor

Article

properties essential for applications across various fields. The diverse compositions and structures of Li-ion oxides provide ample possibilities to explore this crystallography phenomenon, aiming to design battery materials with enhanced performance. This study demonstrates that CSRD arrangements can bolster the capacity retention and structural integrity of cutting-edge oxide cathodes. Characterization and DFT simulations show that integrating local short-range disorder effectively tailors the electrostatic interaction between Co and oxygen, suppressing the detrimental phase transitions and thus promoting structural stability. This differs from previous reports[33,34] using ball milling and element non-stoichiometry to induce partial (dis)order, affecting Li-ion transport. Moreover, this approach also modifies the electronic structure of the materials, enhancing electronic conductivity. Notably, it is observed that the desired phase transition behaviour manifests only when this local disordered structure permeates the bulk of the particles, underscoring its important role in structural stability. This is in contrast to materials with solely surface-disordered structures (Supplementary Fig. 23), which fails to induce the observed structural behaviour exhibited by the CSRD materials.

On charging, Li ions are removed from Li layers, leaving vacancies, which facilitates the possibility of transition metal migration into the Li layers. Here the electronic configuration of the transition metals plays an important part. Transition metal ions with filled t_{2g} levels result in the most stable octahedral environment to resist their migration[35]. In layered oxides, the octahedral cation sites are edge-sharing and face-sharing with the tetrahedral sites. Cation migration between octahedral sites requires moving through an intermediate tetrahedral site, which typically poses a high energy barrier. As for transition metal ions with filled t_{2g} levels, this barrier is raised considerably, immobilizing the transition metal ions. Consequently, the most stable octahedral cation of the $3d$ transition metal ions is low-spin Co^{3+} having the d^6 configuration, which provides a rationale for the improved performances of the CSRD−LiCoO$_2$. This is consistent with the reports on the specific role of Co^{3+} in layered oxide cathodes[36]. Furthermore, high-spin Mn^{4+} in the d^3 configuration also demonstrates considerable octahedral stability due to ligand field stabilization[20]. However, the smaller ionic size of Mn^{4+} ($R_{CN=6} = 0.53$ Å) makes it difficult to be stabilized into Li-ion octahedral sites. By contrast, ions with electronic configurations d^0 (for example, V^{5+} and Cr^{6+}) and d^5 in high spin (for example, Fe^{3+} and Mn^{2+}) are prone to migration across the tetrahedral site[35]. However, some ions, for example, Ti^{4+} can stabilize octahedral structures[37,38], which can thus be used to form CSRD oxides. This is realized in the presently designed CSRD $LiTi_{1/2}Mg_{1/2}O_2$−$LiNi_{0.8}Co_{0.1}Mn_{0.1}O_2$, also considering that $LiTi_{1/2}Mg_{1/2}O_2$ crystallizes in the disordered rock-salt structure. Moreover, we suggest the CSRD in oxide electrodes, when maintained at appropriate concentrations (for example, approximately 2% per unit in this study), could enhance material properties. Given the intricate nature of electrodes during cycling, involving processes such as ion and electron transport, structural evolution and redox behaviour, it is imperative to carefully control the disorder levels in the bulk structure. Here the element properties, the annealing temperature and time, the gas environment, the nature of precursors and the ratio of precursors could be the focus of various materials in future.

Conclusion

In summary, we demonstrate a substantial improvement in the electrochemical performance of Li-ion oxide cathodes by the integration of chemical short-range atomic arrangements. The proof-of-concept study shows that the rationally designed LiCoO$_2$ cathode shows increased cycle life and rate capability when compared with conventional cathodes. This improvement is attributed to the optimized crystal and electronic structure features associated with incorporating local

atomic arrangements. Importantly, these crystallographic characteristics can be extended to more systems, including high-energy-density Ni-rich cathodes, suggesting broader applicability. These findings underscore the significant promise of well-designed short-range atomic arrangements in tailoring the electronic and structural properties of advanced oxide materials and beyond.

Online content

Any methods, additional references, Nature Portfolio reporting summaries, source data, extended data, supplementary information, acknowledgements, peer review information; details of author contributions and competing interests; and statements of data and code availability are available at https://doi.org/10.1038/s41586-024-07362-8.

1. Goodenough, J. B. Evolution of strategies for modern rechargeable batteries. *Acc. Chem. Res.* **46**, 1053–1061 (2013).
2. Mizushima, K., Jones, P. C., Wiseman, P. J. & Goodenough, J. B. Li$_x$CoO$_2$ (0 < x ≤ 1): a new cathode material for batteries of high energy density. *Mater. Res. Bull.* **15**, 783–789 (1980).
3. Reed, J., Ceder, G. & Van Der Ven, A. Layered-to-Spinel Phase Transition in Li$_x$MnO$_2$. *Electrochem. Solid-State Lett.* **4**, A78 (2001).
4. Reimers, J. N. & Dahn, J. R. Electrochemical and in situ X-ray diffraction studies of lithium intercalation in Li$_x$CoO$_2$. *J. Electrochem. Soc.* **139**, 2091–2097 (1992).
5. Elliott, S. R. in *Physics of Amorphous Materials* 2nd edn 139–151 (Longman, 1990).
6. Greer, A. L. in *Intermetallic Compounds—Principles and Practice* Vol. 1 (eds Westbrook, J. H. & Fleischer, R. L.) 731–754 (Wiley, 1995).
7. Sheng, H. W., Luo, W. K., Alamgir, F. M., Bai, J. M. & Ma, E. Atomic packing and short-to-medium-range order in metallic glasses. *Nature* **439**, 419–425 (2006).
8. Zhang, N. et al. The missing boundary in the phase diagram of PbZr$_{1-x}$Ti$_x$O$_3$. *Nat. Commun.* **5**, 5231 (2014).
9. Yang, T. et al. Multicomponent intermetallic nanoparticles and superb mechanical behaviors of complex alloys. *Science* **362**, 933–937 (2018).
10. Zhang, R. et al. Short-range order and its impact on the CrCoNi medium-entropy alloy. *Nature* **581**, 283–287 (2020).
11. Lee, J. et al. Unlocking the potential of cation-disordered oxides for rechargeable lithium batteries. *Science* **343**, 519–522 (2014).
12. Zhao, C. et al. Rational design of layered oxide materials for sodium-ion batteries. *Science* **370**, 708–711 (2020).
13. Cartledge, G. H. Studies on the periodic system. I. The ionic potential as a periodic function. *J. Am. Chem. Soc.* **50**, 2855–2863 (1928).
14. Wang, Q. et al. Designing lithium halide solid electrolytes. *Nat. Commun.* **15**, 1050 (2024).
15. Antaya, M., Cearns, K., Preston, J. S., Reimers, J. N. & Dahn, J. R. In situ growth of layered, spinel, and rock-salt LiCoO$_2$ by laser ablation deposition. *J. Appl. Phys.* **76**, 2799–2806 (1994).
16. Kanno, R. et al. Synthesis, structure, and electrochemical properties of a new lithium iron oxide, LiFeO$_2$, with a corrugated layer structure. *J. Electrochem. Soc.* **143**, 2435–2441 (1996).
17. Sakurai, Y., Arai, H. & Yamaki, J. Preparation of electrochemically active α-LiFeO$_2$ at low temperature. *Solid State Ion.* **113-115**, 29–34 (1998).
18. Werder, D. J., Chen, C. H., Cava, R. J. & Batlogg, B. Diffraction evidence for oxygen-vacancy ordering in annealed Ba$_2$YCu$_3$O$_{7-\delta}$ (0.3 ≤ δ ≤ 0.4) superconductors. *Phys. Rev. B* **37**, 2317–2319 (1988).
19. Li, L. et al. Evolution of short-range order and its effects on the plastic deformation behavior of single crystals of the equiatomic Cr-Co-Ni medium-entropy alloy. *Acta Mater.* **243**, 118537 (2023).
20. Yang, J. H., Kim, H. & Ceder, G. Insights into layered oxide cathodes for rechargeable batteries. *Molecules* **26**, 3173 (2021).
21. Rossen, E., Reimers, J. N. & Dahn, J. R. Synthesis and electrochemistry of spinel LT-LiCoO$_2$. *Solid State Ionics* **62**, 53–60 (1993).
22. Gummow, R. J., Thackeray, M. M., David, W. I. F. & Hull, S. Structure and electrochemistry of lithium cobalt oxide synthesised at 400 °C. *Mater. Res. Bull.* **27**, 327–337 (1992).
23. Hua, W. et al. Chemical and structural evolution during the synthesis of layered Li(Ni,Co,Mn)O$_2$ oxides. *Chem. Mater.* **32**, 4984–4997 (2020).
24. Duffiet, M. et al. Probing Al distribution in LiCo$_{0.96}$Al$_{0.04}$O$_2$ materials using ^{7}Li, ^{27}Al, and ^{59}Co MAS NMR combined with synchrotron X-ray diffraction. *Inorg. Chem.* **59**, 2890–2899 (2020).
25. Zhao, C., Avdeev, M., Chen, L. & Hu, Y.-S. An O3-type oxide with low sodium content as the phase-transition-free anode for sodium-ion batteries. *Angew. Chem. Int. Ed.* **57**, 7056–7060 (2018).
26. Ménétrier, M., Saadoune, I., Levasseur, S. & Delmas, C. The insulator-metal transition upon lithium deintercalation from LiCoO$_2$: electronic properties and ^{7}Li NMR study. *J. Mater. Chem.* **9**, 1135–1140 (1999).
27. Zhang, J.-N. et al. Trace doping of multiple elements enables stable battery cycling of LiCoO$_2$ at 4.6 V. *Nat. Energy* **4**, 594–603 (2019).
28. Yang, X. et al. Pushing lithium cobalt oxides to 4.7 V by lattice-matched interfacial engineering. *Adv. Energy Mater.* **12**, 2200197 (2022).
29. Yang, X. et al. Enabling stable high-voltage LiCoO$_2$ operation by using synergetic interfacial modification strategy. *Adv. Funct. Mater.* **30**, 2004664 (2020).

30. Shao-Horn, Y., Levasseur, S., Weill, F. & Delmas, C. Probing lithium and vacancy ordering in O3 layered $Li_x CoO_2$ ($x \approx 0.5$): an electron diffraction study. *J. Electrochem. Soc.* **150**, A366 (2003).

31. Chen, Z., Lu, Z. & Dahn, J. R. Staging phase transitions in $Li_x CoO_2$. *J. Electrochem. Soc.* **149**, A1604 (2002).

32. Amatucci, G. G., Tarascon, J. M. & Klein, L. C. CoO_2, the end member of the $Li_x CoO_2$ solid solution. *J. Electrochem. Soc.* **143**, 1114–1123 (1996).

33. Lee, J. et al. Reversible Mn^{2+}/Mn^{4+} double redox in lithium-excess cathode materials. *Nature* **556**, 185–190 (2018).

34. Ji, H. et al. Ultrahigh power and energy density in partially ordered lithium-ion cathode materials. *Nat. Energy* **5**, 213–221 (2020).

35. Reed, J. & Ceder, G. Role of electronic structure in the susceptibility of metastable transition-metal oxide structures to transformation. *Chem. Rev.* **104**, 4513–4534 (2004).

36. Zsoldos, E. S., Cormier, M. M. E., Ball, M., Rathore, D. & Dahn, J. R. The effects of small amounts of cobalt in $LiNi_{1-x}Co_xO_2$ on lithium-ion diffusion. *J. Electrochem. Soc.* **170**, 070502 (2023).

37. Wang, Q. et al. Fast-charge high-voltage layered cathodes for sodium-ion batteries. *Nat. Sustain.* **7**, 338–347 (2024).

38. Yabuuchi, N. et al. Origin of stabilization and destabilization in solid-state redox reaction of oxide ions for lithium-ion batteries. *Nat. Commun.* **7**, 13814 (2016).

Article

Methods

Materials

All materials were synthesized using the co-precipitation method coupled with a solid-state reaction. Initially, a specific quantity of alkaline aqueous solution was introduced into deionized water to form the base solution in a tank reactor, which was continuously stirred. Subsequently, a 2 M solution of $CoSO_4 \cdot 7H_2O$, along with an alkaline aqueous solution of 5 M NH_4OH and 10 M NaOH were gradually added to the base solution in the tank reactor at a steady rate of about 8–10 ml min^{-1}. The co-precipitation temperature was maintained at 50 °C and the pH value was regulated at approximately 11 by NH_4OH with a stirring speed of 500 rpm under an N_2 atmosphere. The co-precipitated $Co(OH)_2$ precursor was prepared, which was subsequently washed with deionized water and ethanol four times and dried in a vacuum at 120 °C for 24 h in an Ar atmosphere. For the preparation of CSRD−$LiCoO_2$ materials, the as-obtained precursor was blended with $LiOH \cdot H_2O$ at a molar ratio of 1:1.03; then first heated at 700 °C for 12 h in air and subsequently calcined at 1,000 °C for 6 h in an O_2 atmosphere with a second ground in an agate mortar. The heating rates of the powders were 2 °C min^{-1} and 5 °C min^{-1}, respectively. After cooling naturally, the resulting material was directly transferred into an Ar-filled glovebox to prevent exposure to moisture. The control $LiCoO_2$ material was mixed with $LiOH \cdot H_2O$ at a molar ratio of 1:1.03; and then heated at 950 °C for 12 h. The two-step calcining process is based on the results of operando high-temperature diffraction measurements as shown in Supplementary Fig. 15c. These measurements showed the formation of a rock-salt disordered phase in the temperature range of 400–600 °C, indicating its potential for maximizing the disordered atomic arrangement in this temperature range. Taking into account the disparity between the operando experiment and the synthesis of materials, such as the precursor quantities and heating apparatus, it was concluded that the initial heating step to 700 °C for 12 h favoured the formation of the desired disordered arrangement. Subsequent calcination at 1,000 °C in an O_2 atmosphere facilitated the transformation of the sample into a layered structure. This relatively brief duration of 6 h at an elevated temperature of 1,000 °C, compared with 950 °C for the control material, aided in preserving some of the disordered structure within the bulk, facilitated by a rapid heating rate. Moreover, it helped in preventing cation mixing on the surface of the particles.

For the preparation of $Ni_{0.8}Co_{0.1}Mn_{0.1}(OH)_2$ precursors, a 2 M solution of $NiSO_4 \cdot 6H_2O$, $CoSO_4 \cdot 7H_2O$, and $MnSO_4 \cdot H_2O$ with a molar ratio of 8:1:1 was used, along with an alkaline aqueous solution following the same synthesis process. In the preparation of Mg/Ti−$Ni_{0.8}Co_{0.1}Mn_{0.1}(OH)_2$ precursors, 1% in weight nanosized MgO (98%) and 1% in weight nanosized TiO_2 (anatase, 99.5%) were added in the tank reactor. Both NCM811 materials were mixed with $LiOH \cdot H_2O$ at a molar ratio of 1:1.05; then first heated at 500 °C for 5 h and subsequently calcined at 780 °C for 12 h in an O_2 atmosphere. On natural cooling, the resulting material was promptly transferred into an Ar-filled glovebox to prevent any moisture exposition. Graphite was obtained from BTR New Material Group, by mixing the active material, conductive carbon (Super P) and PVDF conductive carbon in a weight ratio of 94:3:3. The resulting slurry was coated on the Cu foil and subsequently dried at 60 °C for 6 h, followed by drying overnight at 100 °C in a vacuum oven.

Electrochemical measurements

Cathodes were prepared by mixing the active material, Super P and PVDF binder in the mass ratio of 85:7.5:7.5 in N-methyl-2-pyrrolidone solvent. The mixture was then coated onto graphene-coated Al foil and dried at 60 °C for 6 h, followed by further drying in a vacuum oven at 120 °C overnight. Electrochemical cycling tests of all batteries were assembled into CR2032 coin cells in an Ar-filled glovebox (H_2O < 0.1 ppm, O_2 < 0.1 ppm) with a Celgard 2500 separator, unless stated otherwise. Electrolytes (70 µl) were injected into each coin cell

for comparison. All coin cells were tested using multi-channel battery testing systems (Land CT2001A, Lanhe G340A) at room temperature. The electrolyte used was composed of 1 M $LiPF_6$ in a mixture of ethylene carbonate and dimethyl carbonate (DMC) in a ratio of 1:1, with 5% fluoroethylene carbonate (FEC) by volume. Electrochemical performance at higher cutoff voltages (>4.5 V) was tested using an electrolyte consisting of 1 M $LiPF_6$ in a mixture of FEC, methyl (2,2,2-trifluoroethyl) carbonate (FEMC), and 1,1,2,2-tetrafluoroethyl-2,2,3,3-tetrafluoropropylether (TTE) in a 1:1:1 volume ratio, supplemented with 1 wt% LiDFOB as an additive. This electrolyte formulation was chosen to establish a stable electrode–electrolyte interface[29,39]. Galvanostatic intermittent titration technique measurements were conducted using a Maccor instrument, applying repeated current pulses for 30 min at a current density of 0.1 C, followed by a relaxation period of 5 h.

Materials characterization

The morphologies of the materials were analysed using a cold-field SEM (HITACH-SU8010). Powder XRD was conducted using a Bruker D8 Advance diffractometer fitted with a Cu Kα radiation source ($\lambda_1 = 1.54060$ Å and $\lambda_2 = 1.54439$ Å) and a LynxEye_XE detector. Rietveld refinement of the XRD data was performed using the General Structure Analysis System software with the EXPGUI software interface. For in situ XRD studies, the working electrode was prepared using polytetrafluoroethylene as a binder. A specially designed Swagelok cell, equipped with an X-ray transparent Al window, was used for the in situ measurements.

Neutron powder diffraction

NPD data were collected on a high-intensity powder diffractometer (HIPD) at the China Advanced Research Reactor at the China Institute of Atomic Energy. The wavelength was 1.479 Å with a scanning step of 0.05°.

STEM characterization

STEM experiments were performed on a JEM−ARM300F (JEOL) operated at 300 kV with a cold-field emission gun and double Cs correctors. The microscope was equipped with Gatan OneView and K2 cameras for image recording. STEM images were taken with an electron dose rate of 50–500 e^- $Å^{-2}$ s^{-1} with an exposure time for each image for several seconds. EELS spectra were acquired on a GIF Quantum camera with a dispersion of 1 eV per channel, using the dual EELS capability to correct for drift in the low loss centred on the zero-loss peak and core loss centred on the C K-edge. The EELS spectrum images were carried out with a camera length of 20 mm, and a pixel dwell time of 10 ms. Energy drift during spectrum imaging was corrected by centring the zero-loss peak at 0 eV for each pixel. Analysis of the spectra was performed in a Digital Micrograph.

Solid-state NMR characterization

^{59}Co MAS-NMR spectra were recorded on a 400-MHz Bruker ADVANCE III spectrometer (9.4 T magnet) at the ^{59}Co Larmor frequency of 94.94 MHz using a triple-resonance 1.9 mm MAS probe. The spectra were all acquired using a rotor-synchronized Hahn-echo pulse sequence with a π/2 pulse length of 2.0 µs and a recycle interval of 2.0 s. The MAS frequency was 40 kHz and the probe temperature was controlled at room temperature. The transmitter frequency was set to 14,000 ppm. All the ^{59}Co shifts were calibrated using 1 M $K_3[Co(CN)_6]$ solution in H_2O (0 ppm).

First-principles DFT calculations

All the first-principles DFT calculations reported in this study were conducted using the Vienna Ab Initio Simulation Package[40,41] with projector-augmented wave potentials[42] and the Perdew–Burke–Ernzerhof[43] change-correlation functional. A plane-wave basis with a cutoff energy of 520 eV and Γ-centred k-meshes with a density of 8,000 k-points per reciprocal atom was used for all the calculations.

All the calculations were spin-polarized, with Co atoms initialized in a high-spin ferromagnetic configuration and relaxed to self-consistency. The DFT+U method introduced in ref. 44 was used to treat the localized $3d$ electrons of Co with a U value of 3.3, obtained by fitting to experimental and calculated formation enthalpies in a previous study[45]. To simulate the fully disordered phase of $LiCoO_2$ ($Fm\bar{3}m$), we use a special quasi-random structure method for studying solid-solution energies in a disordered face-centred cubic (FCC) structure[46]. This method has gained widespread acceptance for describing the FCC cation sublattice in rock-salt-type oxides[47].

To study the impact of the short-range atomic arrangement of the CSRD−$LiCoO_2$ phase, a supercell with 12 Li ions, 12 Co ions (with one antisite Co) and 24 O ions (48 atoms in total) was reasonably created based on the experimental information. To simulate the de-lithiation CSRD−$Li_{0.5}CoO_2$, we used a method given in ref. 48 to explore geometrically distinct Li/vacancy configurations on possible de-lithiation sites of $Li_{1-x}CoO_2$ structures at $x = 0.5$. We generated all symmetrically distinct configurations of Li on these sites using the Enum software package in refs. 49,50. Then, the structures were ranked by the total energies, in which the structure with the lowest total energy was selected to study the charge density distribution and electronic structure information of the CSRD−$LiCoO_2$ and the regular $LiCoO_2$ oxides. Crystal structures and charge density distribution were visualized by VESTA[51].

Data availability

The data that support the findings of this study are available in the main text and Supplementary Information. All relevant data are available from the corresponding authors upon request.

39. Fu, A. et al. Enabling interfacial stability of $LiCoO_2$ batteries at an ultrahigh cutoff voltage ≥ 4.65 V *via* a synergetic electrolyte strategy. *J. Mater. Chem. A* **11**, 3703–3716 (2023).
40. Kresse, G. & Furthmüller, J. Efficient iterative schemes for ab initio total-energy calculations using a plane-wave basis set. *Phys. Rev. B* **54**, 11169–11186 (1996).
41. Kresse, G. & Hafner, J. Ab initio molecular dynamics for liquid metals. *Phys. Rev. B* **47**, 558–561 (1993).
42. Blöchl, P. E. Projector augmented-wave method. *Phys. Rev. B* **50**, 17953–17979 (1994).
43. Perdew, J. P., Ernzerhof, M. & Burke, K. Rationale for mixing exact exchange with density functional approximations. *J. Chem. Phys.* **105**, 9982–9985 (1996).
44. Dudarev, S. L., Botton, G. A., Savrasov, S. Y., Humphreys, C. J. & Sutton, A. P. Electron-energy-loss spectra and the structural stability of nickel oxide: an LSDA+U study. *Phys. Rev. B* **57**, 1505–1509 (1998).
45. Wang, L., Maxisch, T. & Ceder, G. Oxidation energies of transition metal oxides within the GGA+U framework. *Phys. Rev. B* **73**, 195107 (2006).
46. Wolverton, C. Crystal structure and stability of complex precipitate phases in Al–Cu–Mg–(Si) and Al–Zn–Mg alloys. *Acta Mater.* **49**, 3129–3142 (2001).
47. Urban, A., Matts, I., Abdellahi, A. & Ceder, G. Computational design and preparation of cation-disordered oxides for high-energy-density Li-ion batteries. *Adv. Energy Mater.* **6**, 1600488 (2016).
48. Yao, Z. et al. Revealing the conversion mechanism of transition metal oxide electrodes during lithiation from first-principles. *Chem. Mater.* **29**, 9011–9022 (2017).
49. Hart, G. L. W., Nelson, L. J. & Forcade, R. W. Generating derivative structures at a fixed concentration. *Comput. Mater. Sci.* **59**, 101–107 (2012).
50. Hart, G. L. W. & Forcade, R. W. Algorithm for generating derivative structures. *Phys. Rev. B* **77**, 224115 (2008).
51. Momma, K. & Izumi, F. *VESTA 3* for three-dimensional visualization of crystal, volumetric and morphology data. *J. Appl. Crystallogr.* **44**, 1272–1276 (2011).